Supplementary information

1 Material charactorization

1.1 Effective elastic properties

For a cubic symmetric lattice cell, three independent entries are included in the effective elastic tensor as follows,

$$C = \begin{bmatrix} C_{11} & C_{12} & C_{12} & 0 & 0 & 0 \\ C_{12} & C_{11} & C_{12} & 0 & 0 & 0 \\ C_{12} & C_{12} & C_{11} & 0 & 0 & 0 \\ 0 & 0 & 0 & C_{44} & 0 & 0 \\ 0 & 0 & 0 & 0 & C_{44} & 0 \\ 0 & 0 & 0 & 0 & 0 & C_{44} \end{bmatrix} \tag{1}$$

The Young's modulus and shear modulus are given as follows,

$$E = \frac{1}{S_{11}} \tag{2}$$

$$G = C_{44} \tag{3}$$

where the tensor S is the inverse of C. As illustrated in **Fig. 1**, the effective Young's modulus and shear modulus in an arbitrary direction are given by,

$$E_{\theta\varphi} = S_{11} - 2\left(S_{11} - S_{12} - \frac{1}{2}S_{44}\right)(l_1^2 l_2^2 + l_1^2 l_3^2 + l_2^2 l_3^2) \tag{4}$$

$$\begin{aligned} G_{\theta\varphi\chi} = {} & 4S_{11}(l_1^2 m_1^2 + l_1^2 m_2^2 + l_2^2 m_3^2) + 8S_{12}(l_1 l_2 m_1 m_2 + l_1 l_3 m_1 m_3 + l_2 l_3 m_2 m_3) \\ & + S_{44}[(l_1 m_2 + l_2 m_1)^2 + (l_1 m_3 + l_3 m_1)^2 + (l_2 m_3 + l_3 m_2)^2] \end{aligned} \tag{5}$$

where,

$$l = \begin{pmatrix} \sin\theta\cos\varphi \\ \sin\theta\cos\theta \\ \cos\theta \end{pmatrix};\ m = \begin{pmatrix} \cos\theta\cos\varphi\cos\chi - \sin\varphi\sin\chi \\ \cos\theta\sin\varphi\cos\chi + \cos\varphi\sin\chi \\ -\sin\theta\cos\chi \end{pmatrix} \tag{6}$$

1.2 Poisson's ratio

For a cubic symmetric celluar material, the Poisson's ratio v_s is given as follows,

$$v_s = \frac{C_{12}}{(C_{11} + C_{12})} \tag{7}$$

1.3 Zener's ratio

The Zener ratio has well-accepted as an index to quantify the anisotropy property of a material. For a cubic symmetric celluar material, the Zener's ratio is given as follows,

$$Z = \frac{E}{2G(1 + +v_s)} = \frac{C_{11} - C_{12}}{2C_{44}} \tag{8}$$

1.4 Voigt upper bound

The Voigt upper bounds (VU) represent the theoretical limits of the effective Young's modulus and yield strength for anisotropic celluar materials, which are given as follows,

$$E^{VU} = E_S\bar{\rho} \tag{9}$$

$$\sigma_y^{VU} = \sigma_{ys}\bar{\rho} \tag{10}$$

where $\bar{\rho}$ is the relative density, E_S, σ_{ys}, the Young's modulus, and yield strength of the constituent material, respectively

1.5 Hashin-Shtrikman upper bound

The Hashin-Shtrikman upper bound (HSU) for the effective Young's modulus is the theoretical limit for isotropic cellular materials. For a cubic symmetric lattice material, the E^{HSU} is given as follows,

$$E^{HSU} = \frac{2E_S\bar{\rho}(7-5v_s)}{15(\bar{\rho}-1)v_s^2 + 2(\bar{\rho}-6)v_s - 13\bar{\rho} + 27} \tag{11}$$

1.6 Suquet upper bound

The Suquet upper bound (SU) for the effective yield strength is the theoretical limit for isotropic cellular materials. For a cubic symmetric lattice material, the σ_y^{SU} is given as follows,

$$\sigma_y^{SU} = \frac{6\sigma_{ys}\bar{\rho}}{\sqrt{69-33\bar{\rho}}} \tag{12}$$

1.7 Gibson-Ashby scaling power-law fit

The Gibson-Ashby scaling power-law fit is used to quantify the deformation mode of cellular materials, which is stated as,

$$E/E_S = C\bar{\rho}^n \tag{13}$$

where C is the scaling coefficient, and n is the scaling exponent. For the stretching-dominated lattice, n equals to 1. While for bending-dominated lattice, n equals to 2.

2 Optimization algorithm

2.1 ODE-driven level-set density method

Regarding optimization algorithm, a novel ordinary differential equation (ODE) driven level-set density method was employed to drive optimization. Due to the powerful topological variation ability, this method usually give birth to better optimization results. The method is a combination of level-set and density method. The level-set function (LSF) ϕ is used to describe the structural interface by extracting the zero level-set from the level-set function, which is parameterized as follows,

$$\begin{cases} \phi(\mathbf{X}) > 0 & \forall \mathbf{X} \in \Omega \backslash \partial\Omega \\ \phi(\mathbf{X}) = 0 & \forall \mathbf{X} \in \partial\Omega \\ \phi(\mathbf{X}) < 0 & \forall \mathbf{X} \in D \backslash \Omega \end{cases} \tag{14}$$

where $\mathbf{X}$ is the coordinate of a point inside the design domain D and $\partial\Omega$ is the boundary of the solid domain Ω. The density field is used to develop physical interpolation model, which is shifted from the level-set function. For the proposed method, an exact Heaviside function $H(\phi)$ is used to map the level-set function onto a physical interpolation model,

$$H(\phi) = \begin{cases} 1 & \text{if } \phi \geq 0 \\ 0 & \text{if } \phi < 0 \end{cases} \tag{15}$$

The transformation of the density field ρ_e from the level-set function is given as:

$$\rho_e = \frac{\int_{D_e} H(\phi) d\Omega}{\int_{D_e} d\Omega} \tag{16}$$

where D_e is the element domain. We use a power law penalization scheme to interpolate the element stiffness E_e,

$$E_e(\rho_e) = E_{min} + (\rho_e)^p (E_0 - E_{min}) \tag{17}$$

where E_{min} is the stiffness of weak material, p the penalty factor, and E_0 the stiffness of the element with full material.

The LSF evolution is driven based on nodal sensitivity. Here, the nodal sensitivity V_{NS} is defined as the average sum of the sensitivities of the elements that contain the node, which is given as follows:

$$V_{NS} = \frac{1}{n_e}\sum\nolimits_{1}^{n_e}\frac{\partial C}{\partial \rho_e} \tag{18}$$

where n_e is the total number of elements that share a common node. We use gradient-based method to solve the optimization problem. The Lagrangian function for the mathematical model is formed as,

$$L = C + \Lambda\left(\sum\nolimits_{\mathrm{e}=1}^{N_e}\rho_e v_e - A_f\right) \tag{19}$$

where Λ is the Lagrangian multiplier. According to the Karush–Kuhn–Tucker (KKT) conditions, by differentiating the Lagrangian function with respect to the design variable, the convergence optimal criteria can be obtained as:

$$\frac{\partial C}{\partial \rho_e} + \Lambda = 0 \tag{20}$$

Herein, to deduce the LSF evolution governing ODE, we first investigate a more general spatial motion of LSF. Consider a nD space, the LSF $\phi(\mathbf{X})$ is a function defined in the nD space and can propagate in any direction of the nD space, where $\mathbf{X} = (x_1, \cdots x_j, \cdots, x_n)$. Introducing the pseudo time t, the zero level-set can be written as,

$$\phi(\mathbf{X}, t) = 0\,. \tag{21}$$

By differentiating the LSF with respect to pseudo time t, we have,

$$\frac{\partial \phi}{\partial t} + \frac{\partial \phi}{\partial x_1}\frac{\partial x_1}{\partial t} + \cdots + \frac{\partial \phi}{\partial x_j}\frac{\partial x_j}{\partial t} + \cdots + \frac{\partial \phi}{\partial x_n}\frac{\partial x_n}{\partial t} = 0\,. \tag{22}$$

Herein, if ϕ is immutable along the jth direction in the nD space, i.e., $\partial\phi/\partial x_j = 0$, then Eq.(22) yields,

$$\frac{\partial \phi}{\partial t} + \frac{\partial \phi}{\partial x_1}\frac{\partial x_1}{\partial t} + \cdots + \frac{\partial \phi}{\partial x_{j-1}}\frac{\partial x_{j-1}}{\partial t} + \frac{\partial \phi}{\partial x_{j+1}}\frac{\partial x_{j+1}}{\partial t} + \cdots + \frac{\partial \phi}{\partial x_n}\frac{\partial x_n}{\partial t} = 0\,. \tag{23}$$

But if the value of ϕ only changes along the jth direction in the nD space, it has,

$$\frac{\partial \phi}{\partial x_1} = \cdots = \frac{\partial \phi}{\partial x_{j-1}} = \frac{\partial \phi}{\partial x_{j+1}} = \cdots = \frac{\partial \phi}{\partial x_n} = 0\,, \tag{24}$$

and Eq.(22) becomes,

$$\frac{\partial \phi}{\partial t} + \frac{\partial \phi}{\partial x_j}\frac{\partial x_j}{\partial t} = 0\,. \tag{25}$$

Typically, identify a 3D space and suppose $\phi(\mathbf{X})$ is a function defined in the 3D space where $\mathbf{X} = (x, y, z)$. If only the movements along x and y directions deliver changes of ϕ in the nD space, i.e., $\partial\phi/\partial z = 0$, then Eq.(22) yields,

$$\frac{\partial \phi}{\partial t} + \frac{\partial \phi}{\partial x}\frac{\partial x}{\partial t} + \frac{\partial \phi}{\partial y}\frac{\partial y}{\partial t} = 0\,, \tag{26}$$

which is the classic conventional Hamilton-Jacobi (H-J) partial derivative equation (PDE) for a 2D design problem where structural domain locates in the x-y plane.

Now let us change the way of movement of ϕ, e.g. assuming ϕ is only changeable just along the z direction (i.e., $\partial\phi/\partial x = 0$ and $\partial\phi/\partial y = 0$), we have,

$$\frac{\partial \phi}{\partial t} + \frac{\partial \phi}{\partial z}\frac{\partial z}{\partial t} = 0\,. \tag{27}$$

As can be learned, the update of LSF is only determined by information of z direction. Particularly, if $\partial\phi/\partial z$ is a constant, the PDE of Eq.(27) becomes an ODE. We define the update information as velocity V_z, and we obtain,

$$\frac{d\phi}{dt} + V_z = 0\,, \tag{28}$$

Herein, the Eq.(28) is borrowed to update LSF in this paper and after discretization of design domain the nodal sensitivity is used to drive the propagation of LSF, i.e.,

$$\frac{d\phi}{dt} + V_{NS} = 0\,. \tag{29}$$

Thus, the ODE for evolution of LSF is formulated (note here that Eq.(28) is established for any arbitrary point in the design domain and it is naturally applicable for all analysis mesh nodes). By the introduction of nodal sensitivity, the evolution of

LSF can be used for optimization of structure. However, the volume constraint and convergence evaluation is not incorporated in Eq.(29). Consider the optimal criteria, it is easy to prove that the optimal criteria for elements is equivalent for nodes, hence, based on the elemental optimal criteria in Eq.(20), the nodal optimal criteria can be attained as follows,

$$V_{NS} + \Lambda = 0\,. \tag{30}$$

Replace V_{NS} in Eq.(29) with $V_{NS} + \Lambda$, we have,

$$\frac{d\phi}{dt} + (V_{NS} + \Lambda) = 0\,. \tag{31}$$

Eq.(31) delivers such message that the Lagrangian multiplier Λ is introduced to tackle material volume constraint, and the LSF stops propagating as the optimal criteria term $(V_{NS} + \Lambda)$ becomes 0, in other words, theoretically, the evolution of LSF ends up with all nodal sensitivities equal to the same constant of Lagrangian multiplier, which is a KKT point. Thus, based on Eq.(31), the iterative update format of LSF can be developed as follows,

$$\phi_{i+1} = \phi_i - \Delta t(V_{NS} + \Lambda)\,, \tag{32}$$

where i is the iteration number and Δt is the chosen time step. The stopping criteria for the optimization can be the minimum change of objective function R (compared with, e.g., the last five iterations), or a user-defined maximum loop, i.e.,

$$\frac{|R_i - R_{i-5}|}{R_i} < 1 \times 10^{-4}\,, \text{or } i > \text{loop}_{max}\,. \tag{33}$$

As optimization goes by, though the LSF will stop varying based on the convergence criteria of Eq.(20), the value of ϕ can be very large. In some cases, this situation may suppress the topological changing ability and the optimization is more likely fallen into local optimum or ill-posed solutions owing to that the value of ϕ is limited to change along the direction perpendicular to the structure interface. As a result, the topological variations, such as structural formation, disappearance, translation, rotation, merging and so on, are achieved simply based on the LSF ϕ to grow above or below the cutting level-set, which is different from conventional level-set methods where the LSF is evolved based on normal perturbations of boundaries. Here, to counter numerical issues during optimization process, we propose a regularization scheme as follows,

$$\phi^* = \alpha\phi\,,\ \ 0 < \alpha < 1 \tag{34}$$

where α is a positive scaling factor. The regularization is a linear scaling manner, which works as a re-initialization strategy. By periodically re-initializing the level-set function, the topological defects can be naturally, effectively, and efficiently eliminated, making the optimization more active and responsive.

We adopt the full material design as the initial design to perform optimization as it can ensure broader design space. The given material area G_i at each iteration step is linearly relaxed from the initial full material design, which takes the following form,

$$G_i = A_0 - \left(A_0 - A_f\right)\frac{i}{N_R} \quad i \le N_R \tag{35}$$

where A_0 is the initial material area fraction equal to 1 when choosing the initial design with full material, N_R the prescribed relaxation steps to control material area variation.

For the case of minimization of compliance, the derivative of objective function with respect to design variable can be written as,

$$\frac{\partial C}{\partial \rho_e} = -p(\rho_e)^{p-1}\mathbf{u}_e^T\mathbf{K}_e\mathbf{u}_e \tag{36}$$

2.2 Optimization process

The flowchart for the optimization algorithm is illustrated in **Fig. 2a**. The basic procedures for the optimization include preparation, optimization, and postprocess. In the preparation part, the design variable, design domain, objective, constrains, material property, algorithm parameter, and boundary condition are defined, and the design domain is meshed. In the optimization part, the optimization problem is iteratively solved and the structural design is updated. Finally, the converged design is subjected to postprocess.

2.3 Boundary condition

As the multilayer configurations cause complexity in structural boundaries, the boundary conditions need to be identified clearly. To fully exploit the symmetry of the initial design configuration of a unit cell to save computation cost, the 1/8 divisions for the initial designs are applied to perform optimization. For example, **Fig. 2b** illustrates the boundary condition definition for the Schwarz P-set under uniaxial loading. Three types of boundary conditions are identified, including the displacement boundary, force boundary, and periodic boundary. For a unit cell, the periodic boundary is replaced with free boundary.

3 Practical implementation

To carry out the whole modeling, optimization, and numerical simulation, a series of tools are employed in practical implementation. As demonstrated in **Fig. 2c**, we first use MATLAB to generate the candidate cell surface according to the analytical expression and then construct the initial multilayer design, which is a '.stl' document. Then the geometrical document is obtained based on the '.stl' document. Then the geometrical document is meshed in HYPERMESH. Note here the mesh needs to be fine enough to ensure sufficient optimization design space since the design variable density is mesh element based. After that, the topology optimization is carried out in MATLAB and optimized results are attained, using our home-made code based on the ODE-driven level-set density method. Again, the optimized '.stl' document is remodeled and the geometrical model is meshed. Here, the mesh for the optimized model does not have to be too dense. On the contrary, a coarse mesh helps save computation cost with sufficient proficiency for numerical simulation and verification, which is implemented in commercial software ABAQUS and COMSOL.

4 Method verification

To ensure correctness and effectiveness of the whole method, several analysis techniques need to be verified. In the physical field analysis part of topology optimization, the hybrid element combining membrane element with DKQ plate element is applied to perform the finite element analysis, and the accuracy is verified in comparison with the ABAQUS results. As demonstrated in **Fig. 3a**, for the same benchmark case, the offset of our result from the ABAQUS result is 0.086%. The static simulation with periodic boundary condition was applied to calculate the elastic constants. Also, the quasistatic compressing method was used to study the constitutive relationships of the unit cells. The material iron (Young's modulus: 210GPa, yield strength: 400MPa) is assigned to all unit cells. Both static and quasistatic methods are applied to calibrate the material constitute properties. As displayed in **Fig. 3b** and **Fig. 3c**, the calculated results are consistent with the given material properties, certifying the validity of the analysis method. We study shell-based lattice at low density in this work. The precision and effectiveness of analysis element is verified. The stress-strain constitutive relationships at different densities are investigated with both shell and solid elements. As compared in **Fig. 3d**, the offset of results from shell element and solid element is negligible at low densities, but showing enlarging trend as the relative density increases (with increasing component thickness). Therefore, the shell element can ensure sufficient accuracy for lattices at low densities. The mesh convergence is verified. As shown in **Fig. 3e**, four meshes with different densities are examined for the same benchmark problem, and the calculated results basically show the same with each other.

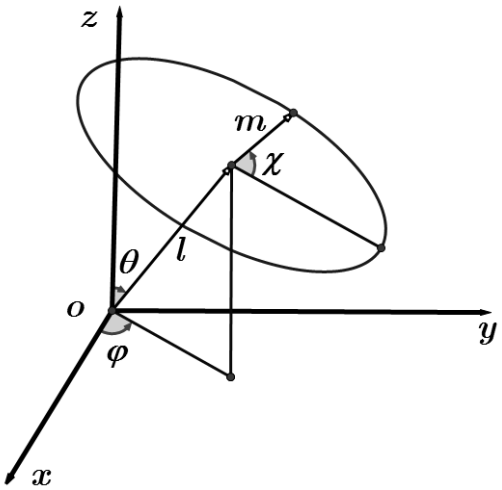

Fig. 1 | Young's modulus and shear modulus in in an arbitrary direction

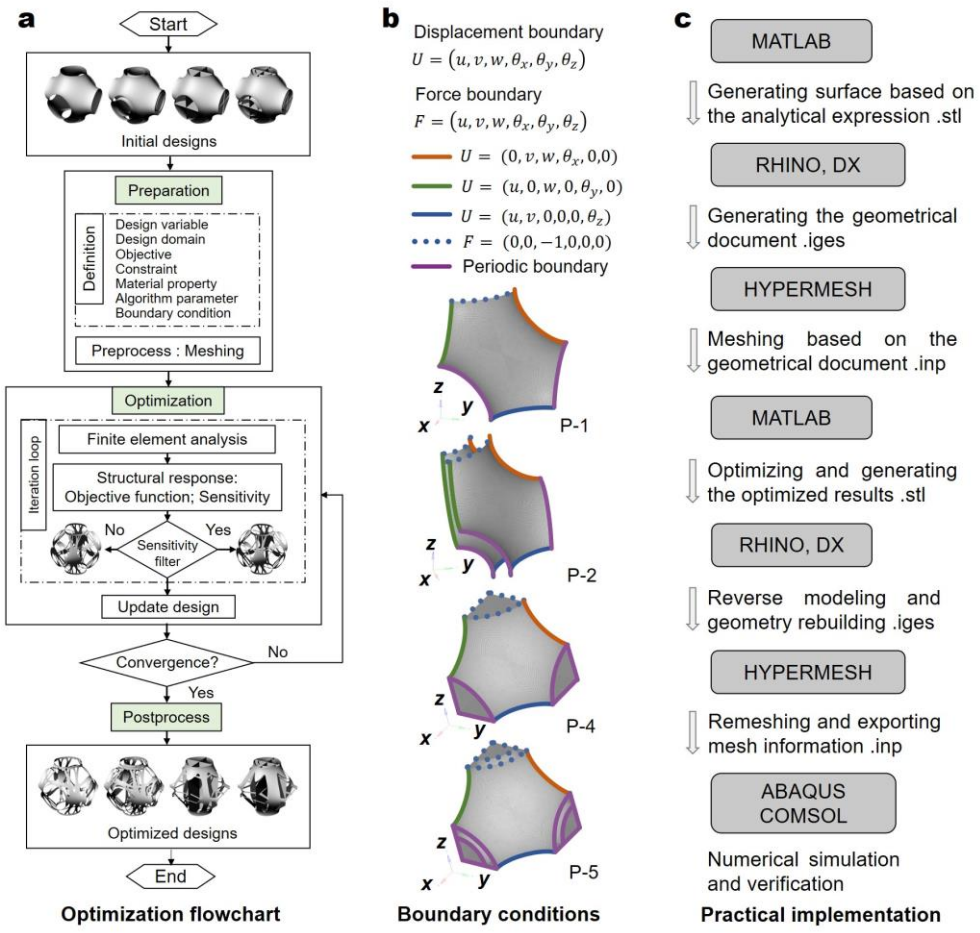

Fig. 2 | Design and optimization strategy for multilayer shell-based lattice. a, optimization flowchart. **b**, definition of boundary conditions. **c**, practical implementation.

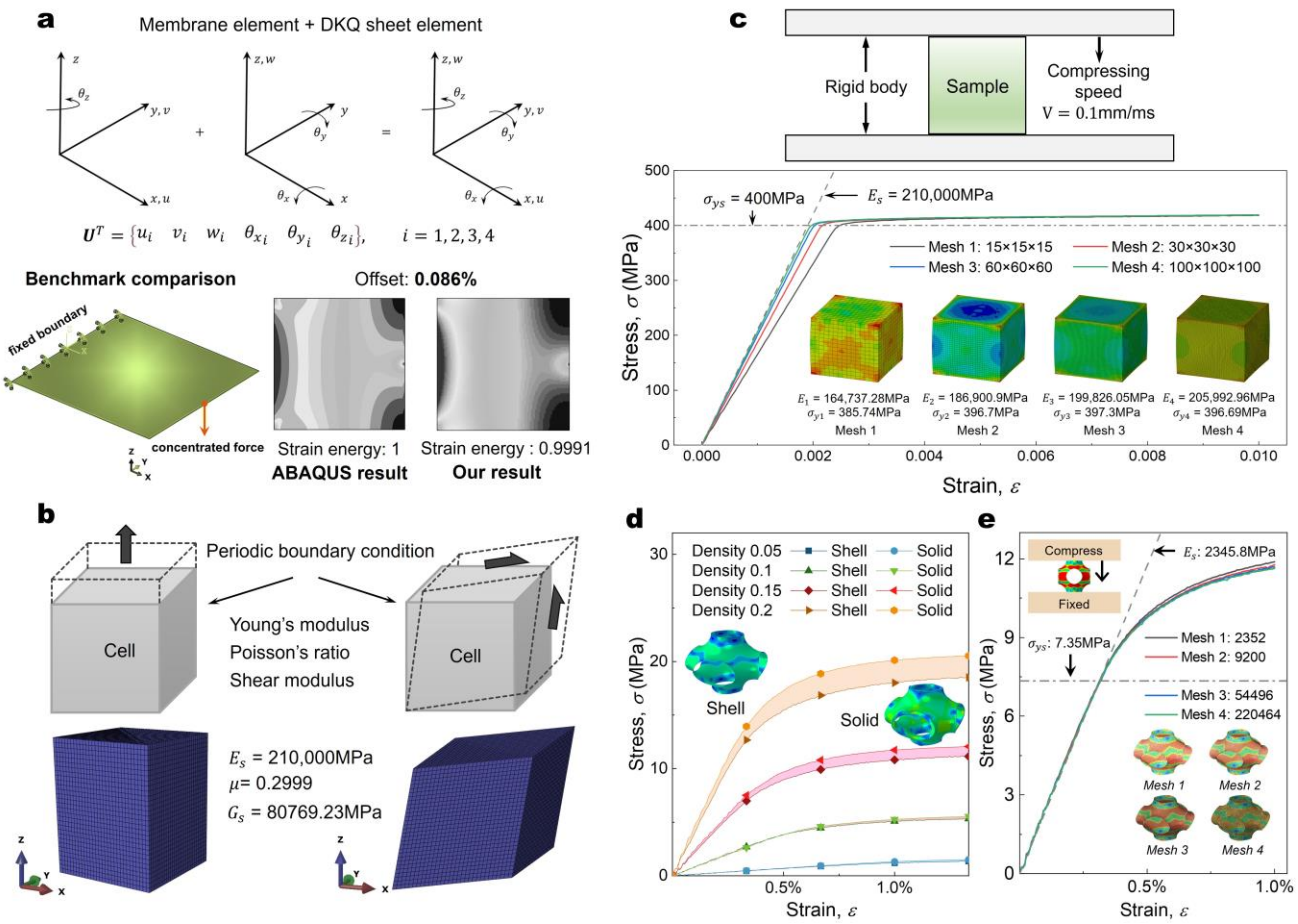

Fig. 3 | Method verification. **a**, verification of element precision. **b**, verification of material property through static analysis method. **c**, verification of material property through quasistatic compressing method based on explicit dynamic computation. **d**, verification of element type. **e**, verification of mesh convergence.

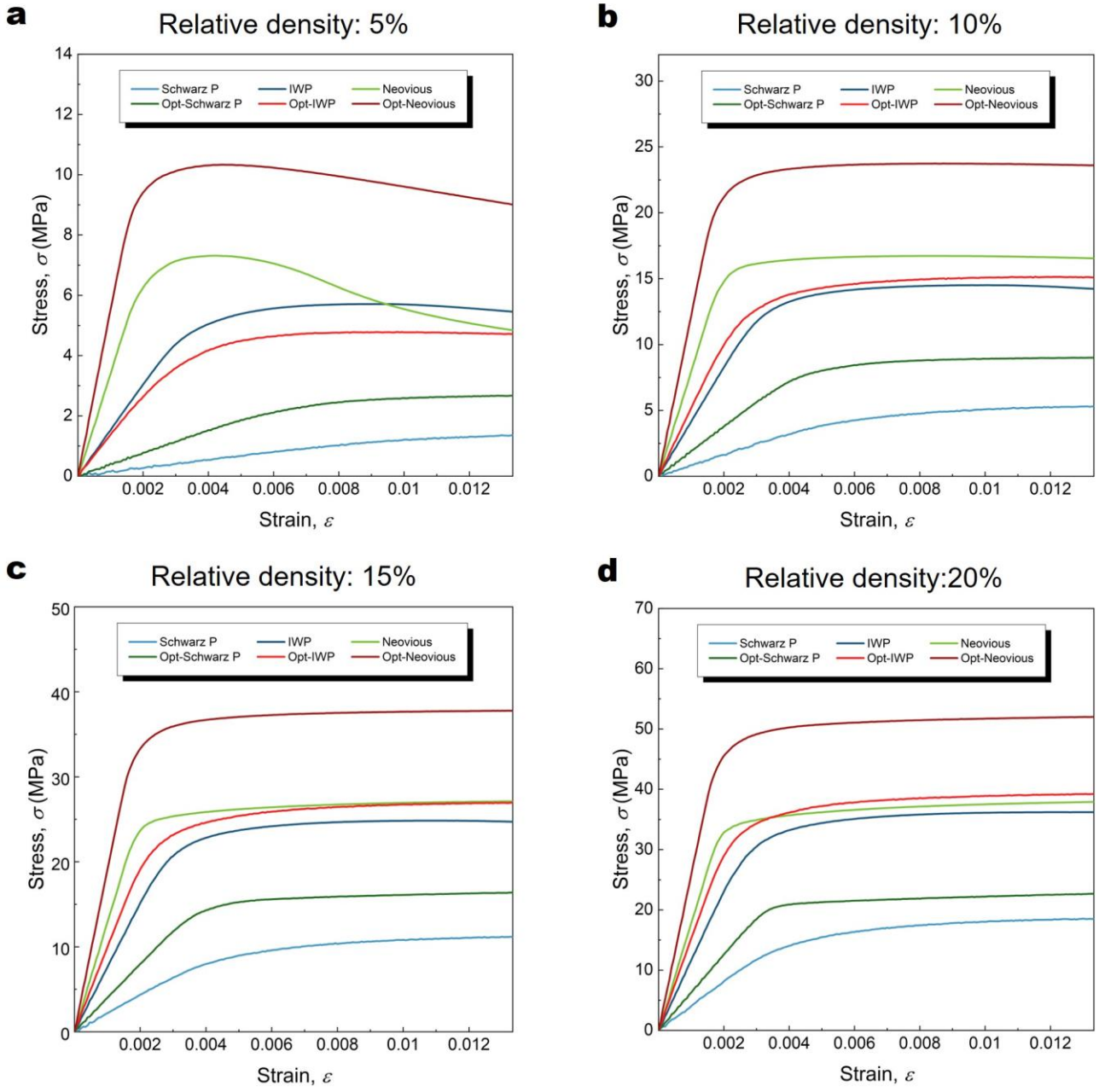

Fig. 4 | Stress-strain curves for Schwarz P, IWP, Neovius, and their optimized results with different relative densities. **a**-**d**, stress-strain curves for relative density 5%, 10%, 15%, and 20%, respectively.

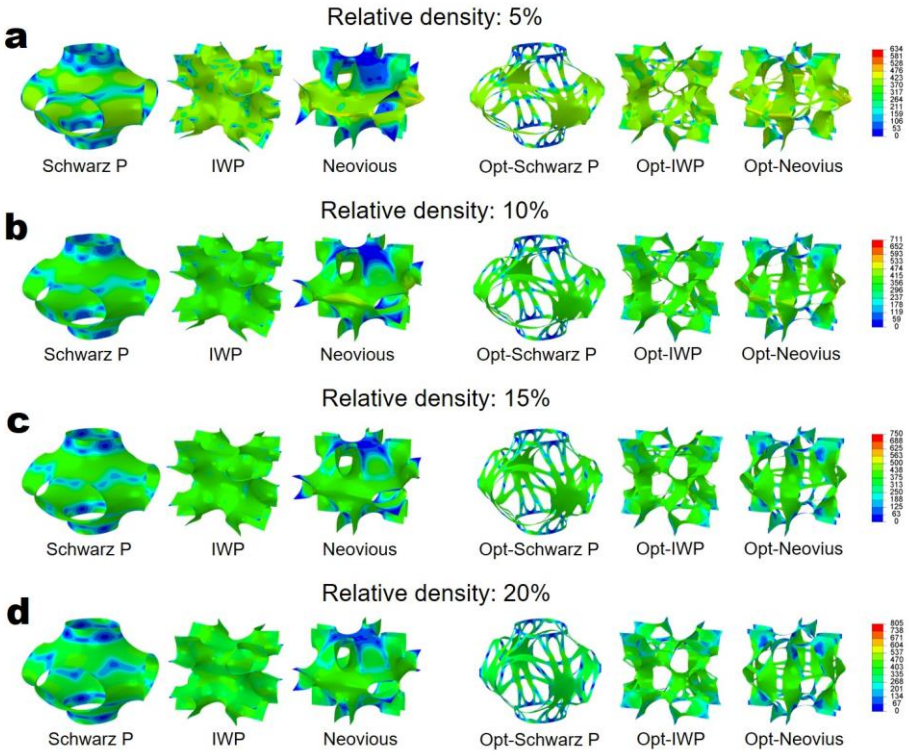

Fig. 5 | Uniaxial deformation for Schwarz P, IWP, Neovius, and their optimized results with different relative densities. **a**-**d**, uniaxial deformation for relative density 5%, 10%, 15%, and 20%, respectively.

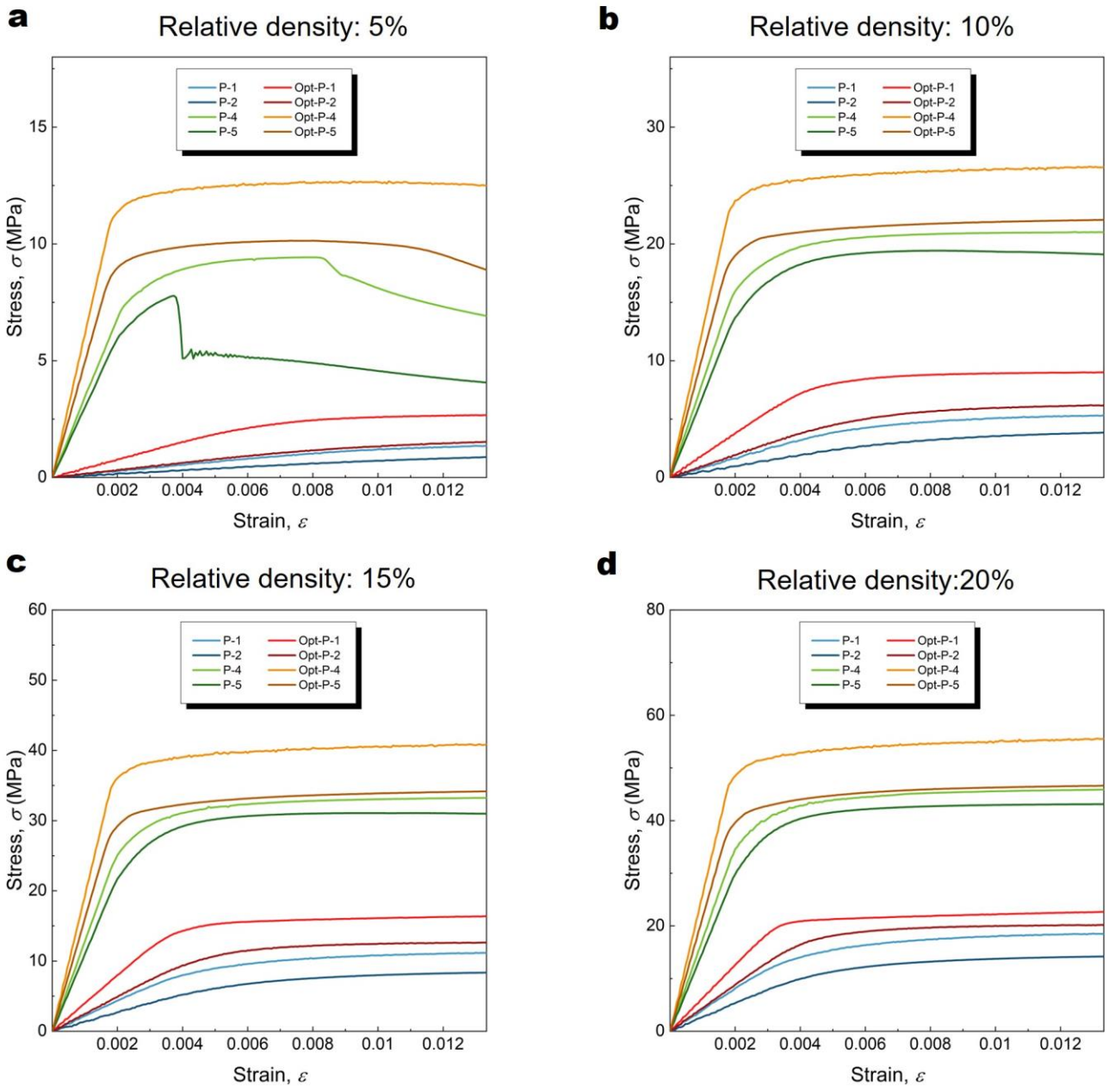

Fig. 6 | Stress-strain curves for Schwarz P and its multilayer variants and their optimized results under uniaxial loading with different relative densities. **a**-**d**, stress-strain curves for relative density 5%, 10%, 15%, and 20%, respectively.

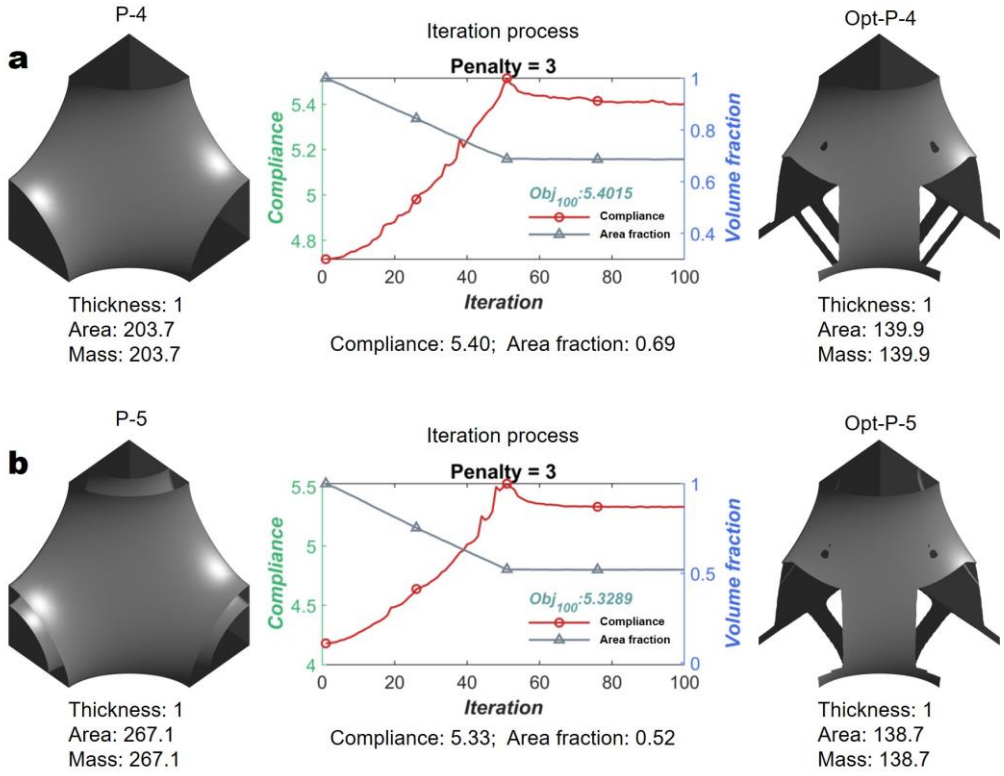

Fig. 7 | Optimization comparison for P-4 and P-5. **a**, optimization for P-4. **b**, optimization for P-5.

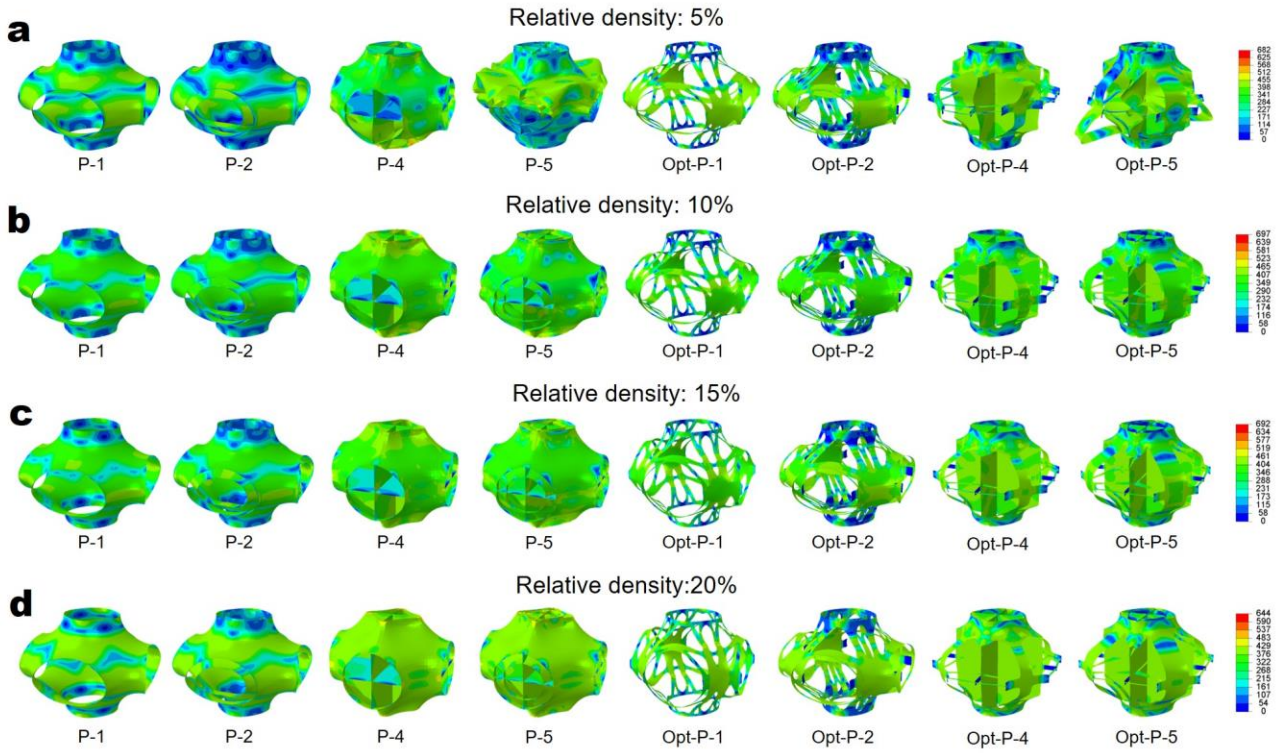

Fig. 8 | Uniaxial deformation for the P set and their optimized results with different relative densities. **a**-**d**, uniaxial deformation for relative density 5%, 10%, 15%, and 20%, respectively.

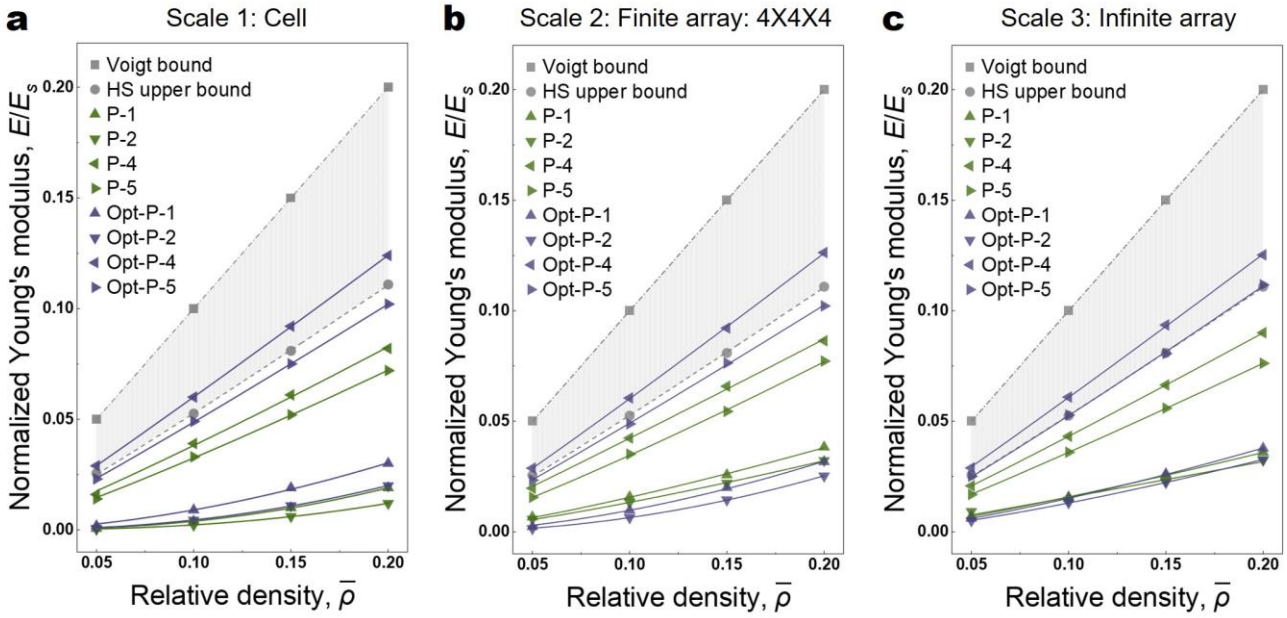

d Gibson-Ashby scaling power law fit: E/E_s $[F(\bar{\rho})^m]$

Model	Cell	Finite array: 4X4X4	Infinite array
P-1	$0.738(\bar{\rho})^{2.272}$	$0.301(\bar{\rho})^{1.285}$	$0.241(\bar{\rho})^{1.184}$
P-2	$0.586(\bar{\rho})^{2.414}$	$0.249(\bar{\rho})^{1.272}$	$0.166(\bar{\rho})^{1.029}$
P-4	$0.499(\bar{\rho})^{1.117}$	$0.466(\bar{\rho})^{1.042}$	$0.495(\bar{\rho})^{1.059}$
P-5	$0.460(\bar{\rho})^{1.151}$	$0.491(\bar{\rho})^{1.152}$	$0.436(\bar{\rho})^{1.084}$
Opt-P-1	$0.504(\bar{\rho})^{1.747}$	$0.503(\bar{\rho})^{1.713}$	$0.317(\bar{\rho})^{1.320}$
Opt-P-2	$0.649(\bar{\rho})^{2.159}$	$0.612(\bar{\rho})^{1.978}$	$0.278(\bar{\rho})^{1.328}$
Opt-P-4	$0.669(\bar{\rho})^{1.047}$	$0.701(\bar{\rho})^{1.066}$	$0.678(\bar{\rho})^{1.047}$
Opt-P-5	$0.567(\bar{\rho})^{1.066}$	$0.566(\bar{\rho})^{1.062}$	$0.634(\bar{\rho})^{1.082}$

Fig. 9 | Scale effect. **a~c**, normalized Young's moduli versus relative density for the cell, finite array, and infinite array scales, respectively. **d**, comparison of Gibson-Ashby scaling power law fit for the Schwarz P set and their optimized results with different scales.

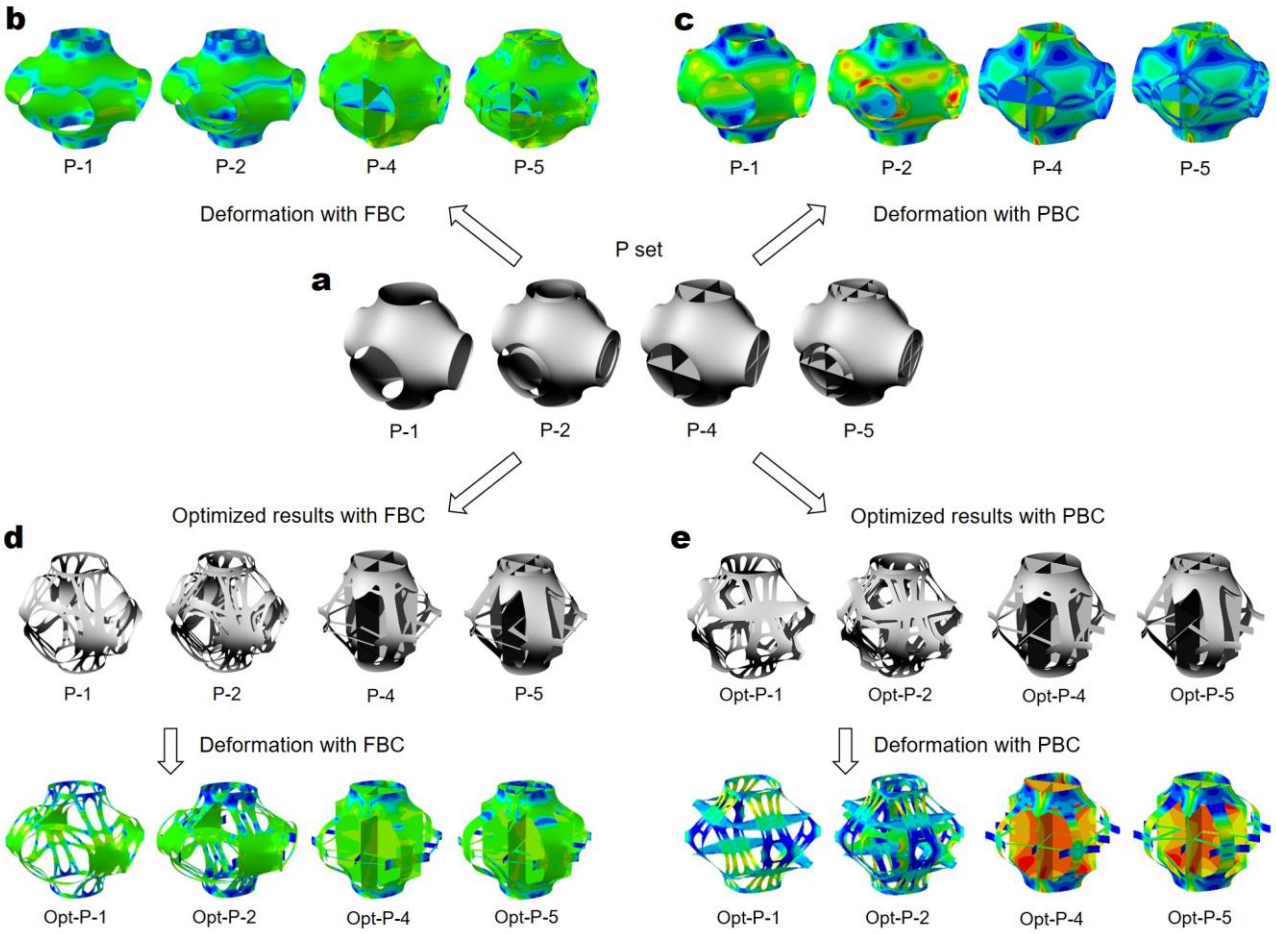

Fig. 10 | Comparison of optimized results with FBC and PBC. a, original Schwarz P set. Subfigures (**b**) and (**c**) compare the deformation modes of Schwarz P set with FBC and PBC, respectively. Subfigures (**d**) and (**e**) compare the optimized results of Schwarz P set with FBC and PBC, respectively. Subfigures (**f**) and (**g**) compare the deformation modes of optimized results of Schwarz P set with FBC and PBC, respectively.

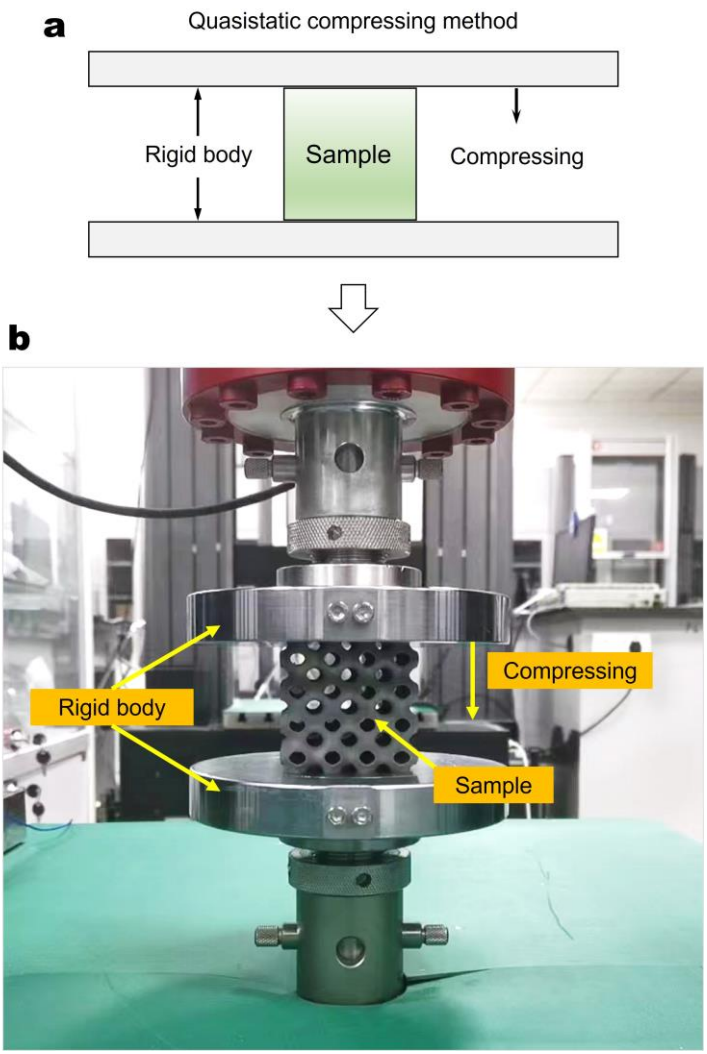

Fig. 11 | Physical situ compressing experiment. **a,** illustration for the quasistatic compressing method. **b,** situ compressing using a universal testing machine.

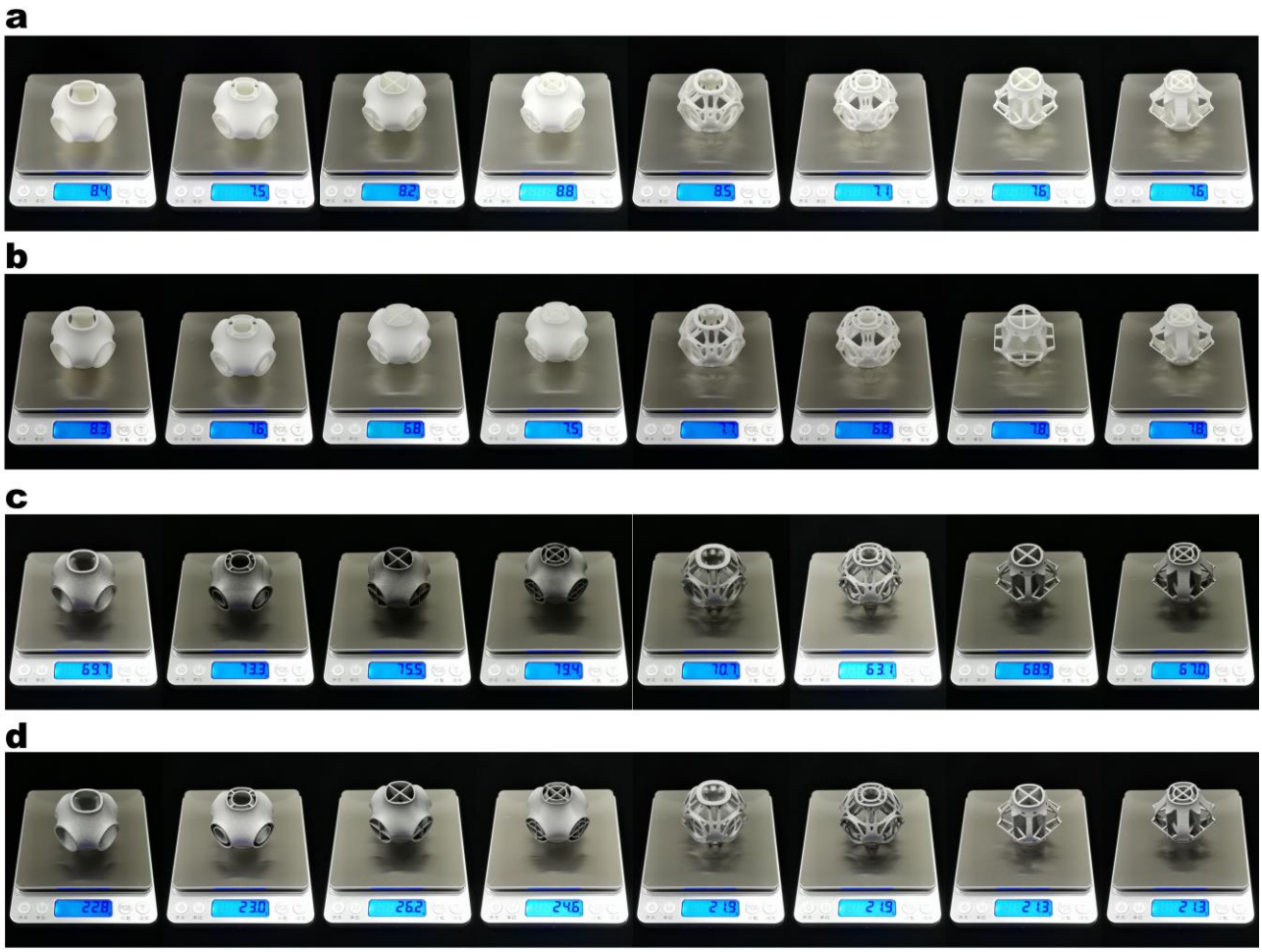

e Mass of printed model (g)

Model	TPU	PA12	SS316	AlSi10Mg
Schwarz P	8.4	8.3	69.7	22.8
Schwarz P-2	7.5	7.6	73.3	23.0
Schwarz P-4	8.2	6.8	75.5	26.2
Schwarz P-5	8.8	7.5	79.4	24.6
Opt-Schwarz P	8.5	7.7	70.7	21.9
Opt-Schwarz P-2	7.1	6.8	63.1	21.9
Opt-Schwarz P-4	7.6	7.8	68.9	21.3
Opt-Schwarz P-5	7.6	7.8	67.0	21.3

Fig. 12 | Fabricated cell models and mass comparison. **a**-**d**, printed cell models with TPU, PA12, SS316, and AlSi10Mg, respectively. **d**, comparison of mass with different materials.

a

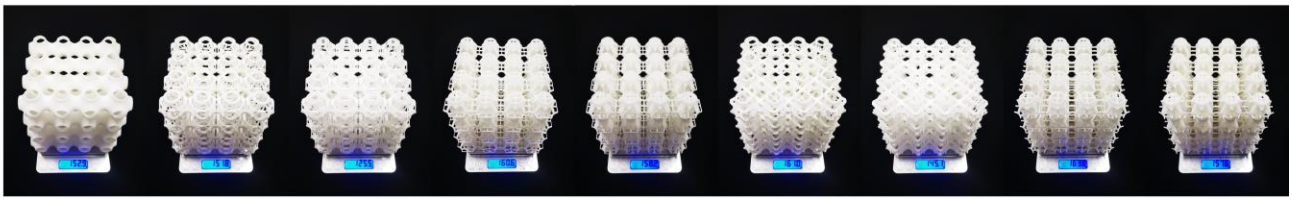

b

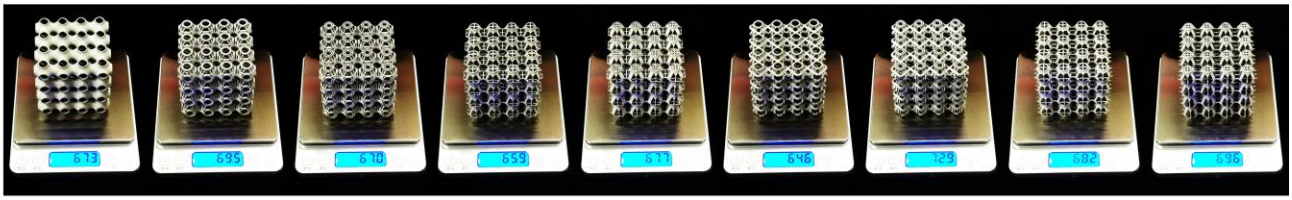

c Mass of printed model (g)

Model	PA12	AlSi10Mg
Schwarz P	152.9	67.3
FBC-Opt-Schwarz P	151.8	69.5
FBC-Opt-Schwarz P-2	125.5	67.0
FBC-Opt-Schwarz P-4	160.6	65.9
FBC-Opt-Schwarz P-5	158.2	67.7
PBC-Opt-Schwarz P	161.0	64.6
PBC-Opt-Schwarz P-2	145.1	72.9
PBC-Opt-Schwarz P-4	163.8	68.2
PBC-Opt-Schwarz P-5	157.6	69.6

Fig. 13 | Fabricated 4X4X4 array models and mass comparison. a-**b**, printed 4X4X4 array models with PA12 and AlSi10Mg, respectively. **c**, comparison of mass with different materials.

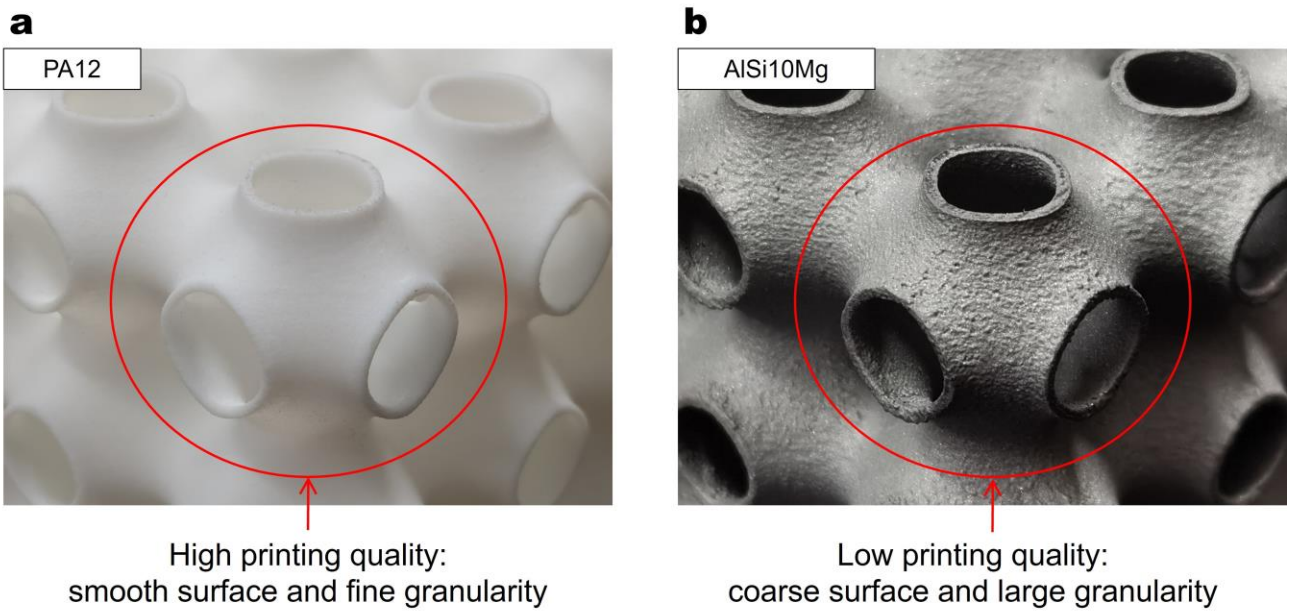

Fig. 14 | Printing quality comparison for 4X4X4 array models fabricated with PA12 and AlSi10Mg. a, printed models with PA12. **b**, printed models with AlSi10Mg.

Table 1 Young's moduli and yield strengths comparison for different single-layer based models (MPa)

Model	Relative density							
	5%		10%		15%		20%	
	Young's modulus	Yield strength	Young's modulus	Yield strength	Young's modulus	Yield strength	Young's modulus	Yield strength
Schwarz P	139.34	1.05	813.24	3.89	2128.1	7.54	4038.9	12.35
IWP	1495.9	3.99	4121.9	10.77	7569	18.94	11504	25.64
Neovius	3391.5	5.43	8003	13.61	12727	21.79	17799	30.37
Opt-H-Schwarz P	194.68	1.1	821.21	3.34	1866.7	6.1	3077.2	10.67
Opt-H-IWP	584.65	1.56	1818.2	4.48	3435.3	8.02	5496.2	10.63
Opt-H-Neovius	2491.6	4.15	5103	8.85	8024.1	13.37	11118	17.79
Opt-A-Schwarz P	381.98	1.92	1880.3	7.01	3967.3	19.11	6304.9	27.54
Opt-A-IWP	1336.7	3.01	4975.5	10.25	9820.1	19.11	15191	27.54
Opt-A-Neovius	5496.6	8.51	12167	19.1	18938	29.98	25815	39.44

Table 2 Young's moduli and yield strengths comparison for Schwarz P set and Opt-Schwarz P set (MPa)

Model	Relative density							
	5%		10%		15%		20%	
	Young's modulus	Yield strength	Young's modulus	Yield strength	Young's modulus	Yield strength	Young's modulus	Yield strength
Schwarz P	139.34	1.05	813.24	3.89	2128.1	7.54	4038.9	12.35
Schwarz P-2	69.22	0.8	465.46	2.54	1270.6	5.68	2523.9	9.76
Schwarz P-4	3400.7	7.03	8087.7	15.64	12757	23.81	17287	34.58
Schwarz P-5	2946.6	6.09	6842.8	13.69	10840	21.68	15057	29.11
Opt-Schwarz P	381.98	1.92	1880.3	7.01	3967.3	12.86	6304.9	18.85
Opt Schwarz P-2	156.11	1.06	917.09	4.34	2344.6	9.38	4266.8	15.36
Opt-Schwarz P-4	6136.8	10.64	12607	22.69	19232	34.62	25968	46.74
Opt Schwarz P-5	4905.6	8.18	10274	17.81	15787	27.37	21377	37.05

Table 3 Numerical and experimental Young's moduli comparison for fabricated cell models (MPa)

Model	Numerical simulation	TPU	PA12	SS316	AlSi10Mg
Schwarz P	813.24	0.064	1.83	320.40	176.00
Schwarz P-2	465.46	0.039	1.79	258.05	103.83
Schwarz P-4	8087.7	0.98	34.8	1403.60	993.67
Schwarz P-5	6842.8	0.69	31.5	1574.31	781.48
Opt-Schwarz P	1880.3	0.21	8.85	634.24	404.19
Opt-Schwarz P-2	917.09	0.085	3.65	431.42	212.25
Opt-Schwarz P-4	12607	1.65	59.35	1938.88	1472.81
Opt-Schwarz P-5	10274	1.09	45.8	2001.96	1350.25

Table 4 Numerical and experimental Young's moduli comparison for fabricated 4X4X4 array models (MPa)

Model (PA12)	Numerical simulation	4X4X4-FBC	Numerical simulation	4X4X4-PBC
Schwarz P	3314.69	13.43	3314.69	13.49
Opt-Schwarz P	2040.75	8.59	3154.69	15.18
Opt-Schwarz P-2	1349.03	2.36	2769.53	8.89
Opt-Schwarz P-4	12718.21	49.2	12790.53	51.11
Opt-Schwarz P-5	10251.31	39.72	11086.41	44.2

Table 5 Numerical and experimental Young's moduli comparison for fabricated 4X4X4 array models (MPa)

Model (AlSi10Mg)	Numerical simulation	4X4X4-FBC	Numerical simulation	4X4X4-PBC
Schwarz P	3314.69	870.73	3314.69	865
Opt-Schwarz P	2040.75	834.18	3154.69	813.21
Opt-Schwarz P-2	1349.03	512.16	2769.53	795.71
Opt-Schwarz P-4	12718.21	1730.44	12790.53	1888.77
Opt-Schwarz P-5	10251.31	1747.34	11086.41	1609.89

Table 6 Elastoplastic relationship of the given material of iron

Stress (MPa)	Plastic strain
400	0
429.825	0.0114319
462.573	0.0290993
535.088	0.0748268
642.69	0.151732
729.24	0.22448
766.667	0.265012
797.076	0.302425
825.146	0.345035
836.842	0.36582

Table 7 Material property of aluminum

Property	Value
Density	2700 kg/m^3
Young's modulus	70 GPa
Poisson's ratio	0.33
Thermal conductivity	238 W/(m·K)
Heat capacity at constant pressure	900 J/(Kg·K)

Table 8 Material property of air

Property	Value
Density	1.29 kg/m^3
Speed of sound	340 m/s
Relative permittivity	1
Dynamic viscosity	17.9×10^{-6} Pa·s
Thermal conductivity	0.0267 W/(m·K)
Specific gas constant	287 J/(Kg·K)
Heat capacity at constant pressure	1005 J/(Kg·K)